Shape Deformation and Atomization of Functional Droplets in Contact with a Vibrating Surface

P. Deepu[1], Abhishek Saha[2], Saptarshi Basu[1*], Ranganathan Kumar[2]
[1]Indian Institute of Science, India
[2] University of Central Florida, USA
pdeepu@mecheng.iisc.ernet.in, abhishek.saha@ucf.edu, sbasu@mecheng.iisc.ernet.in and ranganathan.kumar@ucf.edu

Abstract

The dynamics of functional sessile droplets placed asymmetrically on the transducer surface of a 100 kHz vibrating surface is studied. Using high-speed imaging, different regimes of spreading and atomization of the droplets are identified. The dynamics of seven different fluids, namely water, nanosilica suspension in water at three different concentrations, glycerol and water/glycerol binary mixtures at two different concentrations at the same amplitude of oscillation was investigated. The effects of fluid viscosity, surface tension and the non-Newtonian behavior of fluids on the droplet dynamics were analyzed. Fluid viscosity was found to strongly influence the droplet spread rate, deformation and emergence of capillary waves that lead to atomization.

Introduction

Droplet dynamics on a vibrating platform has been the topic of research for many investigators. Many papers have reported detailed analysis of the various modes of vibration exhibited by oscillating droplets [1-7]. Studies have also been carried out to find the threshold of the input parameters that result in the atomization of the droplet [2]. Droplet atomization finds applications in fuel injection, spray coating, aerosol-therapy, metal powder production, air-conditioning, humidifiers and various other industrial processes. Among the different atomization methods ultrasonic atomization is found to be very efficient due to the uniform drop size distribution in the resulting spray. Since the droplet deformation plays a very important role in the atomization physics of the droplet, it is crucial to understand the behavior of the droplet that leads to atomization. Acoustic fields have been used to study droplet dynamics [8-12] in connection with applications like cloud physics, acoustic agglomeration, acoustic levitation and containerless processing. In this paper, a study of sessile droplet behavior placed on a vibrating transducer surface of an ultrasonic 100 kHz levitator is carried out. The droplet undergoes different stages of deformation leading to atomization for most fluids. Attention is given to the stage of droplet distortion prior to atomization. The influence of fluid properties on the droplet dynamics is studied using fluids like water, glycerol and mixtures thereof. The presence of colloidal nanoparticles is studied by considering nanosilica fluid at various concentrations. High speed imaging allowed a temporal resolution of 50 μs and spatial resolution of 5 μm. The droplet deformation characteristics are quantified through image analysis and an analytical model is generated to explain the physics of the deformation process.

Experimental Methods

The transducer surface (made of tantalum) of a single axis Tec5 acoustic levitator was used as the vibrating platform for the droplet. The radius of the surface was 3.8 mm. The droplet was positioned manually on the transducer surface at a distance of approximately 1.8 mm from its centre using a microsyringe. The base diameter of the undisturbed droplet was approximately 1.8 mm. A Photron Fastcam SA5 camera fitted with a Navitar microscopic lens (6.5X zoom objective and 1.5X lens attachment) was used to record the deformation process of the droplets at a framing rate of 20000 fps with a pixel resolution of 896 x 392 and 256 grey levels per pixel. When the transducer is turned on, the tantalum surface starts to vibrate at a frequency, f = 100 kHz. In addition to imparting a harmonic force on the droplet, due to the presence of the reflector situated opposite to the transducer in the levitator setup, the oscillating surface establishes a vertical ultrasonic standing wave. Due its off-centric location with respect to the levitator axis, the droplet was subjected to this pressure wave asymmetrically. The droplet was deployed always at the same location at the right side of the levitator axis (as viewed by the camera). The different fluids investigated were: (a) water; (b) colloidal suspension of 20 nm SiO_2 nanoparticle in water at three different volume fractions, namely, 0.27 (referred to hereafter as NS27), 0.1 (NS10) and 0.05 (NS05); (c) glycerol and (d) aqueous solution of glycerol at volume concentrations of 0.2 (GW2080) and 0.9 (GW9010). NS27 suspension was obtained from Alfa Aesar and dilute suspensions were prepared by mixing the original solution with de-ionised water and ultra-sonicating the solution for 30 minutes. Proper care was taken to ensure that the emitter surface was free of any contaminants before each experimental run.

The high speed images were post-processed using image analysis tools in MATLAB. After detecting the droplet contour from an image, the following parameters were evaluated: the contact angle (both at right and left contact points of the droplet with the surface), the dimension of the base of the droplet projected on the viewing plane (henceforth called "base length" for brevity) and the horizontal and vertical positions of the centroid of the droplet projected area. The centroid data will be used in analysing the stages of the droplet deformation and mechanics where the droplet motion is confined to the direction parallel to the viewing plane, where the centroid of droplet area and centre of mass of the droplet volume can be assumed to coincide.

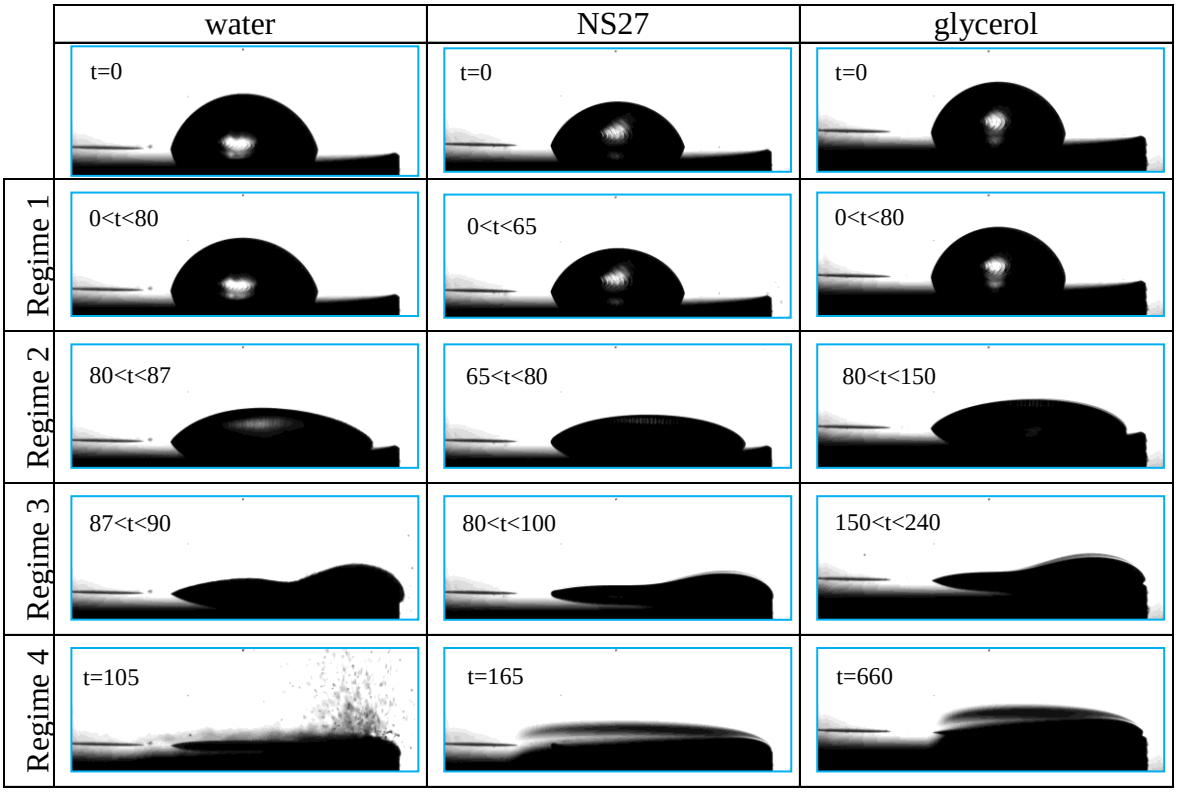

Figure 1 Snapshots showing the chronology of different regimes in the dynamics of droplets of water, NS27 and glycerol on an oscillating surface (f = 100 kHz) in the presence of a standing wave. The figures show an area of around 4.6 mm X 2 mm. The approximate range or instant of time of occurrence in ms of each regime is given in the respective figure (t = 0 represents the start of oscillation of the emitter surface). The different regimes identified are: (1) Small-scale Oscillation Regime; (2) Droplet Spreading Regime; (3) Two-lobe Regime; (4) Film-spreading/Atomization Regime.

Results and Discussion

By examining the images of the droplet subsequent to the beginning of the vibration of the surface, four major regimes could be identified as given in Fig. 1 where the snapshots from the different regimes are reported for water, NS27 and glycerol droplets. The first row of images shows the undisturbed droplet located asymmetrically on the ultrasonic emitter surface. In Regime 1 (immediately after the transducer is turned on) small-amplitude capillary wave begins to appear on the droplet surface. The energy given to the droplet from the transducer surface leads to this small scale capillary waves. The droplet centroid position and the dynamic contact angles, especially the right contact angle, show oscillations in this regime. The contact line remains pinned (retains its circular shape and size) and hence base length does not show any change. Since the duration of this regime is same across all the fluids, it is to be believed that the effect of the standing pressure wave is minimal at this stage. Minimal pressure force fluctuation that may exist across the free boundary of the droplet is balanced by the surface tension force of the droplet. In Regime 2, the pressure field due to the standing wave is strong enough that the droplet starts to move towards the right with its left contact point pinned. This motion has been found to be similar for droplets of all the fluids studied (with same initial base length). The reason for this unidirectional motion is as follows. The effect of acoustic radiation force on the free boundary of the droplet can be resolved into radial (F_r) and vertical (F_z) components as shown in Fig 2. In our experiments, since the droplet is situated in the pressure antinode present at the driving transducer surface, the effect of F_r is to push the droplet radially outwards (i.e., rightwards as per the location of the droplets in the images) and that of F_z is to pull the droplet upwards

vertically upwards [13]. For the F_z component to have considerable influence on the droplet dynamics, it has to overcome the downward gravitational pull, the intermolecular forces existing within the liquid droplet and the force of adhesion between the liquid and the solid supporting surface. On the other hand, the only opposing force for the F_r component is the viscous force within the droplet. Hence the flattening and rightward spreading of the droplet suggests that the droplet distortion in this regime is dominated by the F_r component. Nevertheless, the capillary waves noticed in the later regimes may have been brought up by the combined effect of F_r and F_z. While spreading, the leftward liquid-solid adhesive force acting on the base of the droplet ensures that the no-slip boundary condition is obeyed at the interface. The net result is that the fluid layer adjacent to the surface does not move at all and the free top portion of the droplet starts to deform and move in a pouring action resulting in droplet spreading rightwards (toward the edge) leading to CG shift. This rightward sliding motion of the top mass of droplet over the bottom static layers under the action of the radially outward F_r component and leftward frictional force at the solid-liquid boundary suggests that the left contact point remains pinned while the right contact point moves toward the right. The flexural vibration of the transducer surface may further assist in the motion of the droplet. In order to validate this hypothesis, experiments were carried out with droplets deployed on points diametrically opposite on the surface and they were observed to slide leftwards. The change in time scale of this regime across the different fluids suggests that rate of change of the dynamic base length is dependent on fluid properties. This regime will be analyzed later in detail.

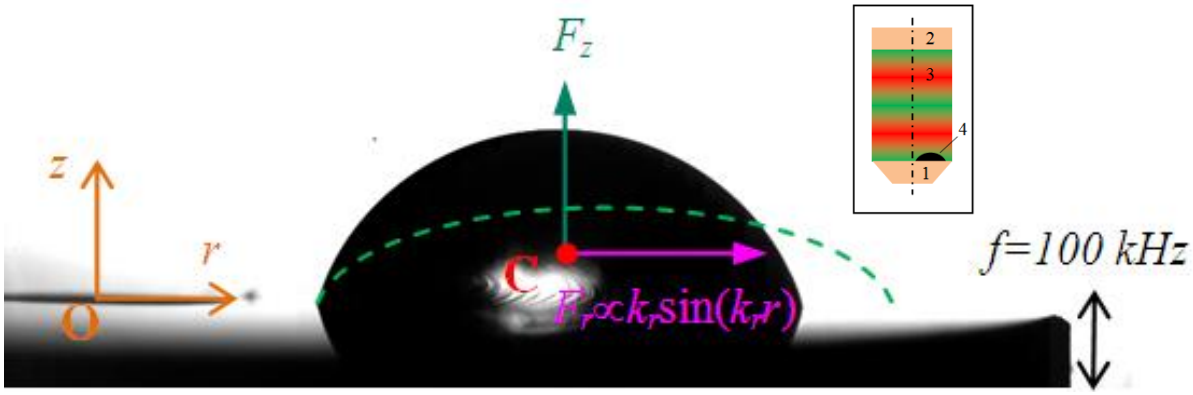

Figure 2 Schematic showing the acoustic forces acting on the sessile droplet in Regime 2. The radial force is represented by a point load (F_r) acting through the C.G. of the droplet, denoted by C. r in the expression for F_r is the distance measured from the centre, O, of the emitter surface [13]. F and k_r are the frequency and radial wave number of the ultrasonic standing wave respectively. The dashed green arc represents the deformed droplet. Inset shows the location of the droplet (4) relative to the standing wave (3) created between the oscillating transducer surface (1) and the reflector (2). The green regions represent pressure antinode and the red regions represent pressure node.

The radially outward momentum gained by the liquid mass in regime 2 pushes the droplet toward the right end of the surface and when the right edge of the droplet reaches the edge of the surface, regime 3 initiates, where the inertia of the liquid mass makes the fluid rush to the right side of the droplet leading to a distinctive bulge. Here, the net effect of the action of the inertia forces, the air-liquid surface tension forces, internal viscous forces and the external pressure forces leads to the two-lobe deformation of the droplet, where the left contact point is still pinned due to the aforementioned reasons. Subsequently, the liquid in the left lobe (under the action of the radial force) gets transferred to the right lobe. In the case of low viscous fluids like water, due to the lesser dissipation of the imparted energy, this process continues until the two lobes get separated. Regime 4 involves further flattening of the right lobe. Fluid from the right lobe starts to run over the surface along the edge in clockwise direction (as looking from the top). The low viscous fluids like water and NS05 show distinctive difference in behavior, in addition to the time scales, from the highly viscous ones like glycerol and NS27 in regimes 3 and 4. Atomization begins from the surface of the right lobe of water and NS05 droplets from the beginning of regime 3 and continues all the way into Regime 4. Hence regimes 3 and 4 lack a clear demarcation in low viscosity fluids. The droplet is further deformed by uneven external pressure distribution near the droplet due to acoustic streaming. A stagnation point is expected to occur at the left side of the droplet whereas the average static pressure acting on the right side of the droplet is very low. The kinetic energy imparted by the streaming air flow past the droplet result in the generation of droplet surface waves overcoming the surface tension of the droplet. As the droplet spreads across the surface, this non-uniformity in pressure increases and when the minimum local radius of curvature of the droplet undergoing deformation decreases below a threshold value, the surface tension force fails to balance the differential pressure force and this imbalance can trigger atomization. More important-

ly, in these later regimes, since the droplet has spread extensively, due to the increased contact area with the vibrating surface and the decreased thickness of the droplet, the effect of the energy pumped by the transducer vibration to the droplet becomes prominent. As a result of these disturbances, high wavenumber multi-modal capillary waves form on the surface of the right lobe. Finer droplets start detaching from the crests of the capillary wave due to Faraday-wave instability and finally the atomization results in the catastrophic break-up of the droplet. The atomization is found to be focused at the part of the right lobe of the droplet which is closest to the free edge of the emitter surface as this end has highest amplitude of oscillation, whereas the left lobe still maintains the spherical cap shape without any sharp curvature and no atomization. On the other hand, the glycerol droplet does not atomize at all due to its high viscosity. The NS27 droplet, which is less viscous than glycerol but more viscous than water, does not atomize until it spreads on the surface and takes the form of a thin film. *The intensity of the atomization process thus decreases with viscosity of the droplets.* This shows that viscosity dampens out disturbances, making the droplet more resistant to deformation and subsequent atomization. The details of atomization regime are beyond the scope of this paper.

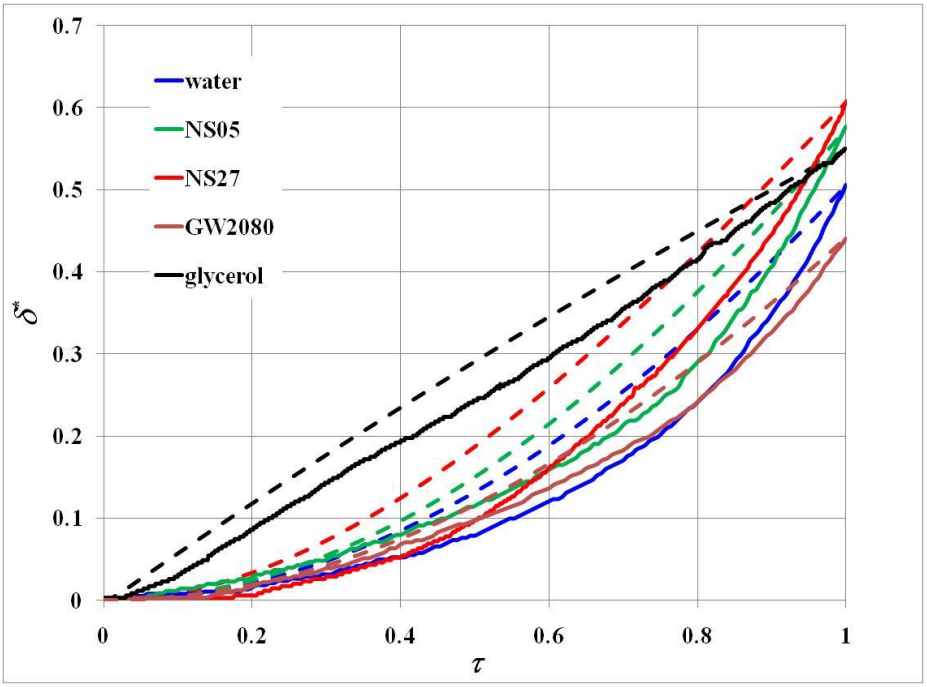

Figure 3 δ versus non-dimensional time. Solid curves represent experimental values and dashed curves represent the simulation results.

Details of Regime 2

The time duration of Regime 2 for the droplets is given in Table 1. Glycerol shows the maximum spreading time. The next highest time scale is for GW9010 and then NS27. Water, NS05, NS10 and GS2080 have similar low values of the spreading time-scale. Since the length across which the droplet spread is maintained constant among all the fluids, the implication is that the speed at which the droplet spreads is different. To understand the dependence of this spread-rate on various parameters, a mathematical model is developed to simulate the droplet distortion. The experimentally observed normalised change in base length of a few droplets, δ^* (= (l-l_i)/l_i, where l is the instantaneous droplet base length and l_i is the initial base length), as a function of time during Regime 2 is given in Fig. 3. The time is normalized by the total time taken by the respective droplets for entire Regime 2. Except glycerol, all other fluids show a similar trend. The rate of change of base length ('spread-rate') is lower at first and gradually it increases. Glycerol almost shows a constant rate of change after a sharp increase during an initial short period of time. The numerical model was formulated by applying law of conservation of linear momentum on the droplet in the horizontal direction (as the dominant force F_r is in horizontal direction). The resulting equation is

$$\ddot{\delta} + C_\mu \frac{\mu_l \bar{l}}{m}\dot{\delta} + C_\sigma \frac{\sigma_{lv}}{m}\delta = \frac{C_F(\tilde{F}_{ri} + \tilde{F}_{rf})}{m}. \quad (1)$$

where δ, μ_l, $\bar{l}$, m, σ_{lv} and $\tilde{F}_r$ stand for the change in base length (l-l_i), fluid viscosity, mean of initial and final droplet base lengths, mass of the droplet, liquid-air surface tension, and the normalized space-averaged acoustic force. Subscripts i and f denote the values at the start and end of Regime 2. m is evaluated by assuming the static droplet to be a spherical cap. The properties of the fluids used are either measured in our lab or taken from the literature [14-16]. Here the droplet base length is considered to be the major dimension that represents the droplet spreading characteristics. The different external forces acting on the droplet are the interfacial forces at the droplet contact line, viscous stress force at the solid liquid boundary and the radial acoustic radiation force. The effective surface tension force at the contact line can be shown to be a function of the instantaneous contact angle and σ_{lv}. For simplicity, the variation of the contact angle as a function of time and across the fluids is not considered in the present analysis. However the constant, C_σ introduced in the surface tension force term impart to the model the average effect of these variations. Similarly in the viscous force term, the constant C_μ incorporates the average dependence on the dynamic contact angle. Additionally, the length scale, $\bar{l}$ incorporated in the viscous force term is the average of the initial and final base-lengths of droplet during the spreading regime. The reason for not taking a itself as the length scale is to maintain the linearity of Equation 1. In addition, although the frequency of oscillation of the emitter surface is 100 kHz, in regime 2, the droplet experiences a pseudo-steady (non-oscillating) force represented by the average RMS pressure force on the droplet. In addition to the radial acoustic force (F_r), there could be other forces acting horizontally on the droplet such as the force due to the roughness of the emitter surface (F_{rough}), force originating from the elastic modes of vibration of the supporting surface ($F_{elastic}$) and the forces due to the transverse stress acting on the droplet due to Poisson effect of the axial component, F_z, of the acoustic force (F_{pois}). But due to the lack of information regarding the values or functional forms of these additional forces, their effect has to be absorbed in the coefficient C_F. Moreover, the predominant component among all these forces is the radial acoustic force, F_r. In order to take into account the variation of the acoustic force experienced by the droplets due to the slight change in their locations and during the spreading process, the right hand side of equation 1 is obtained by taking the average of initial and final values of normalised radial acoustic force at the emitter surface averaged over the droplet base-length, i.e. $\tilde{F}_r \propto \int_l \sin(k_r r)dr/l$, where k_r is the radial wave number of the standing wave. Though the pressure field will be modified due to scattering on the droplet surface and added impedance from the liquid layer, the functional variation of the acoustic force is assumed to be the same.

Table 1. Comparison of the time duration of Regime 1 between numerically obtained values and the experimental values.

Fluid	Actual time scale (ms)	Predicted time scale(ms)
Water	8.5	8.5
NS05	8.25	7.15
NS10	8.8	10.6
NS27	19	10.2 (for μ = 0.05 Pa.s) 19.2 (for μ = 0.2 Pa.s) 35.9(for μ = 0.4 Pa.s)
GW2080	7	10
GW9010	28.9	23.9
Glycerol	69.35	66.4

Initially C_F was taken to be 1 and equation 1 is solved analytically assuming that the excitation is a step function at t =0 and using the initial conditions: $\delta(0) = \dot{\delta}(0) = 0$. By trial and error, the coefficients C_σ and C_μ were tuned to get reasonable match of the results with the observed time scales for glycerol and water as these two fluids represent the extremes of the considered spectrum of fluid properties, mainly viscosity. As the surface tension and viscous forces are found to be the restoring forces, Equation 1 resembles the equation of an excited spring-damper system. But since the maximum value of base length is limited by the size of the emitter surface and the droplet goes into Regime 4 at this limit, no oscillation is observed experimentally, which was also ensured by adjusting the coefficients. Finally the constant C_F is modified so that the model gives the experimental value of δ in the case of water. The modified values of C_σ, C_μ and C_F are 1.1, 0.15 and 0.0001329 N respectively. The theoretical time scales and plots for all the fluids with these same values of the coefficients are also given in

Table 1 and Fig. 3. The theoretical δ^* - τ curves agree with the experimental profiles satisfactorily in the case of all fluids; this proves the functionality of the proposed model. Acceptable agreement of time scales between the analytical and experimental values is observed for all fluids except NS27. For NS27, the results obtained from the model using the dynamic viscosity value of 0.05 Pas (as reported by the vendor) shows significant inconsistency with the observed results. The results from the model address two major questions. First, why does glycerol show a disparity in the δ^*-τ profile as compared to other fluids? Second, why does the time-scale predicted by the model for NS27 does not match with the observed value? Since the simulation result confirms the profile of glycerol, an examination of the different inputs into the model reveals that the disparity in the trend of glycerol curve from that of others can be attributed to its very high viscosity. The low viscous fluids show a sharp increase in spread-rate after a period of time. At the beginning of Regime 1, the non-uniformity of the pressure field across the droplet surface is less due to the spherical shape and hence the droplet surface tension is strong enough to balance this pressure field. But as the droplet starts to spread due to the action of the radial force, the droplet surface area increases and hence the pressure difference across the polar equatorial region of the droplet increases. In order to balance this increased pressure force, the radius of curvature of the droplet has to change as the surface tension remains a constant. This leads to further deformation and spreading of the droplet, resulting in an accelerated change of the droplet base length. But in the case of glycerol the spread-rate increases smoothly without any acute change in slope. The higher viscosity leads to dissipation of energy that the external pressure field imparts on the droplet. Under the action of the external forces glycerol starts to spread, leading to the initial rise in spread-rate. But once it gains enough momentum the internal viscous shear stress builds up to such a level that any further rise in the differential pressure force due to the spreading of droplet leads to only marginal increase in the momentum. The higher viscosity of glycerol leads to an over-damped solution of Equation 2 and hence the model captures the behaviour of glycerol quite accurately. On the other hand, the solution for water and NS05 correspond to the under-damped case and good match is obtained in their cases also. Nevertheless, the rate of change of base length predicted by the model is not as high as the observed value as the model does not take into account the fact that the force increases with time. For instance, the theoretical curve of glycerol shows a decrease in the spread rate over time, whereas in actuality, spread rate increases slightly due to the temporal increase in the magnitude of the external forces.

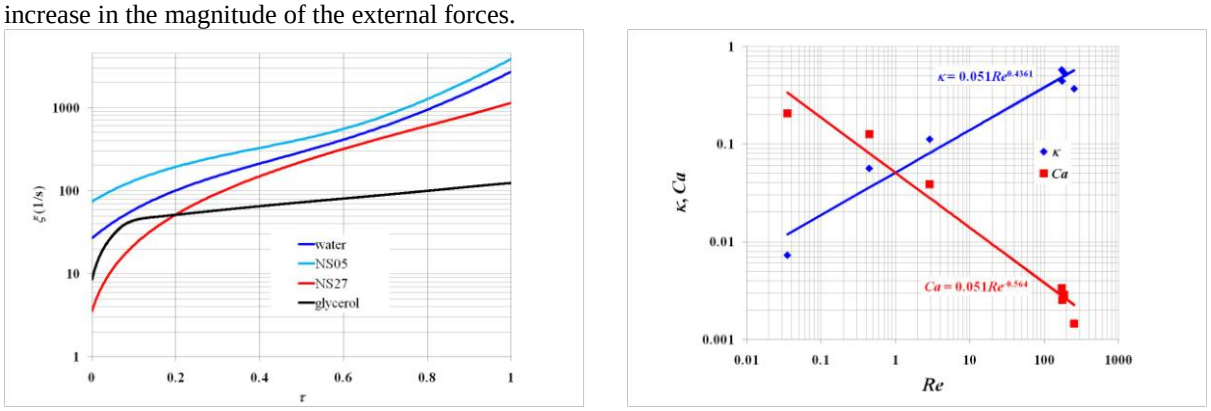

(a) (b)

Figure 4 (a) shear rate versus non-dimensional time (b) Dependence of κ and *Ca* on *Re*.

The mismatch for NS27 can be attributed to its non-Newtonian behaviour [9], where the viscosity of nanosilica colloidal suspension of the same concentration and particle diameter as the one studied here is reported to be dependent on the shear rate. From the spread-rate data and taking the distance from the emitter surface to the centroid of the droplet as the scale in y-direction, shear rate, ξ, for the droplets were estimated and presented in Fig. 4a. It shows that the value of ξ is below 10 s^{-1} for a considerable period of time in Regime 2. Hence the viscosity of the suspension starts at a value much higher (10 times) than 0.05 Pa.s and reduces as the shear rate increases due to shear-thinning phenomenon. If the viscosity is taken to be 0.4 Pa.s as per the data given in [17] for low shear rates, the model gives a time scale that is much higher than the observed value (see Table 1). However, for an intermediate value of viscosity, the time scale matches well. But this viscosity leads to the overdamped profile, whereas the observed profile suggests that the real response is underdamped because it resembles the form of water. Hence the disagreement of NS27 experimental and analytical curves can be attributed to the uncertainty in the value of the viscosity and its variation over time due to the dependence on the shear rate.

Using the non-dimensional variables $\delta^* = \delta / l_i$ and $t^* = t\bar{u} / l_i$ and approximating that $m \sim \rho_l {l_i}^3$ (ρ_l is the fluid density and $\bar{u}$ is the average spread-rate), one may obtain two dimensionless forms of Equation 1 representing two limiting cases as follows: (i) Equation 2 obtained by assuming that the external acoustic force scales

as the inertia force, i.e., $\overline{F} \sim \rho_l \overline{u}^2 l_i^2$ and (ii) Equation 3 obtained by assuming that the external force scales as the viscous force, i.e., $\overline{F} \sim \mu_l \overline{u} l_i$.

$$\frac{d^2\delta^*}{dt^{*2}} + \frac{C_\mu}{Re}\frac{d\delta^*}{dt^*} + \frac{C_\sigma}{\kappa}\delta^* = \frac{\overline{F}}{\rho_l \overline{u}^2 l_i^2}, \tag{2}$$

$$Re\frac{d^2\delta^*}{dt^{*2}} + C_\mu\frac{d\delta^*}{dt^*} + \frac{C_\sigma}{Ca}\delta^* = \frac{\overline{F}}{\mu_l \overline{u} l_i}, \tag{3}$$

where $Re = \frac{\rho_l l_i \overline{u}}{\mu_l}$ is the Reynolds number and $\kappa = \frac{\rho_l l_i \overline{u}^2}{\sigma_{lv}}$ is the modified Weber number (mean kinetic energy normalized by the surface energy). Since both C_σ and C_μ are of order 1, for inertial force dominant spreading, Equation 1 suggests that *Re* must have a directly-proportional relationship with κ (so that the inertia term balances the external force term at high *Re*), whereas for low-*Re* spreading, from Equation 2, it is clear that *Re* and *Ca* must be inversely related. Since our experiments involve intermediate *Re*, both these relationships are expected to hold. From the experimental data (Fig. 4b) the following correlations were deduced:

$$\kappa = 0.051 Re^{0.47}, \qquad Ca = 0.051 Re^{-0.56} \quad \text{for} \quad 0.01 < Re < 100 \text{ and } 0.5 < We_a < 0.7, \tag{4}$$

where $We_a = 2p_0\gamma_0 Ma^2 l_i / \sigma_{lv}$ is the acoustic Weber number based on RMS value of acoustic streaming velocity (p_0 is the atmospheric pressure, γ_0 is the specific heat ratio of air, *Ma* is the acoustic Mach number). Since the surface tension of the fluids do not vary substantially We_a variation is also limited. These correlations present the main features of the spreading process in a nutshell. The fact that glycerol has the least spread-rate is mathematically expressed by the first correlation which states that a fluid with the lowest *Re* will have the least average kinetic energy. The energy imparted on the droplet through the pressure field or the emitter surface oscillations is dampened by the resistive viscous behaviour of the fluid resulting in a lower net droplet deformation rate. At the same time, the higher *Ca*, as per the second correlation also suggests that the whole spreading is basically a viscous force dominated process. The reverse is true for a low viscous fluid like water, for which the process will be dominated by the inertia (high *Re*) and surface tension (low *Ca*) forces.

The left and right dynamic contact angles (Figs. 5a and 5b respectively) were estimated by fitting a straight line through the five consequent pixels on the edge-detected boundary of the droplet in an image at the respective contact points. The five pixel points selected on the droplet edge were separated by a maximum of 3 pixels and this separation was reduced if the slope of the droplet edge is found to be varying sharply near the contact points (for example towards the end of Regime 2) to get an accurate value of the slope of the tangent at the contact point. The contact angle data presented is smoothened to give the generic variation in Regime 2 and normalized with the corresponding value of the static droplet.

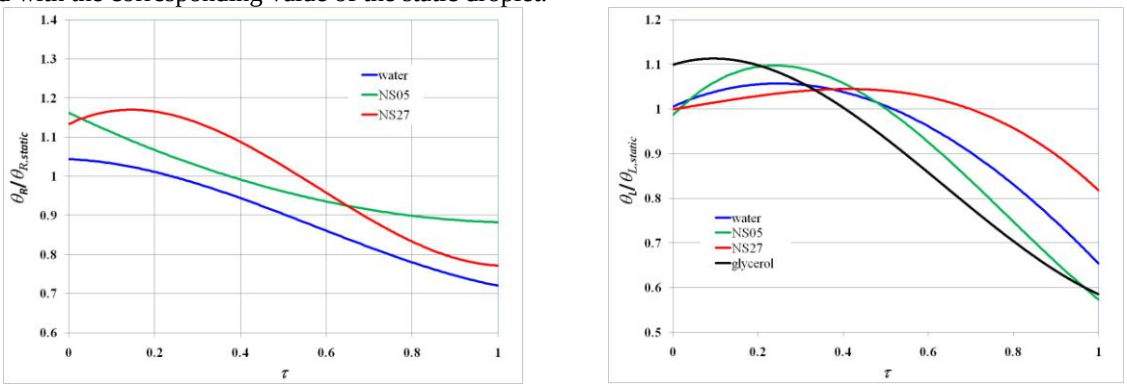

(a) **(b)**

Figure 5 (a) Non-dimensional right contact angle versus non-dimensional time. (b) Non-dimensional left contact angle versus non-dimensional time

The left contact angle of all fluids in found to increase initially because as the right contact point starts to move rightwards, a high-amplitude surface wave starts to emerge from the right side of the droplet which makes its way to the left contact point. The maximum value in the left contact angle coincides with the point when the first crest of the surface wave reaches the left contact point. But at this point the top layers of the droplet have slid rightwards and this bulk motion superimposes on the local variation of right contact angle and hence it starts to decrease from this point. Unlike the permanently pinned left contact point, the right contact point keeps shifting to the edge due to the sliding motion of the top layers. Due to this dynamic behaviour, the measurement of

the right contact angle was more challenging. In the case of glycerol, owing to its high viscosity, the thickness of the boundary layer in contact with the emitter surface is so high that the sliding action is noticeable in the video images. On the other hand, water and NS05 have thinner boundary layers and the sliding motion is smoother.. Their contact angle shows a continuous drop with time and this can be interpreted as the effort of the droplet to dissipate the energy from the external pressure field through deformation. NS27 exhibits an increase in the right contact angle initially. The reason for this can also be explained from Fig. 1. The droplet edge left contact point of the deforming NS27 droplet is not as sharp as that of water or glycerol droplets. This may be due to the formation of a thin layer of agglomerated particles near the emitter surface. This offers a higher resistance for the top layers of the droplet to slide compared to other fluids. Hence the droplet first bulges out on the right side while trying to spread, resulting in an initial increase in the right contact angle. But after the top layers get enough energy to start sliding, the right contact angle begins to decrease. This agglomeration in the boundary layer might be another reason for the mismatch found in the experimental and theoretical time scales for NS27.

Summary and Conclusions

Different stages of droplet deformation were observed due to the standing wave of the levitator and vibrating transducer surface. In this paper, the spreading regime was investigated in detail. The success in simulating the droplet base-length curves using an analytical model indicates that the droplet behaviour is akin to a spring-mass-damper system subjected to a step impulse. Correlations involving the principal non-dimensional parameters are obtained using the experimental results. The droplet spread-rate is found to be a major function of the fluid viscosity. Glycerol exhibited the slowest spread rate while water was the fastest. The atomization regime is due to surface capillary waves formed due to the energy pumped by the transducer surface and the perpendicular radiative pressure field. For further details of this work, readers are referred to [18].

References

[1] Strani, M., Sabetta F., *Journal of Fluid Mechanics* 141: 233-247 (1984).
[2] Vukasinovic, B., Smith, M. K., Glezer, A., *Physics of Fluids* 19, 012104 (2007).
[3] James, A. J., Smith, M. K., Glezer, A., *Journal of Fluid Mechanics* 476: 29-62. (2003).
[4] Morihiro Okada, Minoru Okada, *Experiments in Fluids* 41-5: 789-802 (2006).
[5] Dong, L., Chaudhury, A., Chaudhury, M., *The European Physical Journal E* 21-3: 231-242 (2006).
[6] Noblin, X., Buguin, A., Brochard-Wyart, F., *The European Physical Journal E* 14-4: 395-404 (2004).
[7] James, A. J., Vukasinovic, B., Smith, M. K., Glezer, A., *Journal of Fluid Mechanics* 476: 1-28 (2003).
[8] Trinh, E., Zwern, A., Wang, T. G., *Journal of Fluid Mechanics* 115: 463-474 (1982).
[9] Trinh, E., Zwern, A., Wang, T. G., *Journal of Fluid Mechanics* 122: 316-338 (1982).
[10] Saha, A., Basu, S., Kumar, R., *Journal of Fluid Mechanics* 692: 207-219(2012).
[11] Kumar, R., Tijerino, E., Saha, A. & Basu, S., *Applied Physics Letters* 97, 123106 (2010).
[12] Basu, S., Saha, A., Kumar, R., *Applied Physics Letters* 100, 054101 (2012).
[13] Lierke, E. G., Holitzner, L., *Measurement Science and Technology* 19, 115803 (2008).
[14] Nian-Sheng Cheng, *Industrial & Engineering Chemistry Research 47* (9), 3285-3288 (2008).
[15] Khossravi, D., Connors, K. A., *Journal of Solution Chemistry* 22-4: 321-330 (1993).
[16] Saha, A., Basu, S., Kumar, R., *Experiments in Fluids* 52930: 795-807 (2012).
[17] Venerus, D. C., *et al*, *Applied Rheology* 20-4: 445–462 (2010).
[18] Deepu, P., Basu, S., Saha, A., Kumar, R., *Physical Review Letters*, unpublished.